

High-resolution imaging of C + He collisions using Zeeman deceleration and VUV detection

Vikram Plomp,^{†,§} Xu-Dong Wang,^{†,§} François Lique,^{*,‡} Jacek Kłos,[¶] Jolijn Onvlee,[†] and Sebastiaan Y.T. van de Meerakker^{*,†}

[†]*Radboud University, Institute for Molecules and Materials, Heijendaalseweg 135, 6525 AJ Nijmegen, the Netherlands*

[‡]*Université de Rennes, Institut de Physique de Rennes, 263 avenue du Général Leclerc, 35042 Rennes CEDEX, France*

[¶]*University of Maryland, Department of Physics, Joint Quantum Institute, College Park, MD, United States of America*

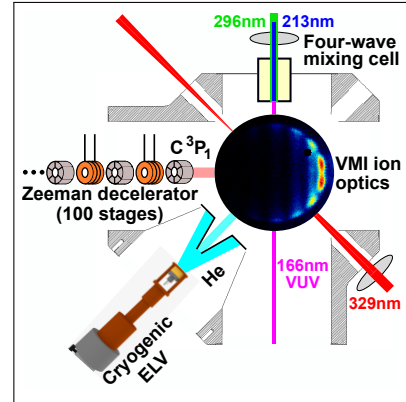
[§]*Contributed equally to this work*

E-mail: francois.lique@univ-rennes1.fr; basvdm@science.ru.nl

Abstract

High-resolution measurements of angular scattering distributions provide a sensitive test for theoretical descriptions of collision processes. Crossed beam experiments employing a decelerator and velocity map imaging have proven successful to probe collision cross sections with extraordinary resolution. However, a prerequisite to exploit these possibilities is the availability of a near-threshold state-selective ionization scheme to detect the collision products, which for many species is either absent or inefficient. We present the first implementation of recoil-free vacuum ultraviolet (VUV) based detection in scattering experiments involving a decelerator and velocity map imaging. This allowed for high-resolution measurements of state-resolved angular scattering distributions for inelastic collisions between Zeeman-decelerated carbon C(3P_1) atoms and helium atoms. We fully resolved diffraction oscillations in the angular distributions, which showed excellent agreement with the distributions predicted by quantum scattering calculations. Our approach offers exciting prospects to investigate a large range of scattering processes with unprecedented precision.

Graphical TOC Entry



The used combination of Zeeman deceleration, (1+1') (VUV+UV) near-threshold REMPI detection and velocity map imaging (VMI) allowed for high-resolution imaging of C-atom scattering distributions after interaction with He.

Acquiring a detailed understanding of molecular interactions is an important goal in physical chemistry.¹ Theoretical descriptions for these interactions have become ever more advanced, and sophisticated experiments have been designed to test their quality.²⁻⁶ In the last decades, crossed beam experiments that studied molecular collisions in the gas phase have provided sensitive probes for the potential energy surfaces (PESs) underlying molecular interactions.⁷⁻¹⁰ One of the most stringent tests for the involved PESs can be found in measurements of angular scattering distributions, which directly reflect the differential cross sections (DCSs).¹¹⁻¹⁵ In this regard, the high resolution afforded by the combination of Stark^{16,17} or Zeeman^{16,18,19} deceleration to control collision partners and velocity map imaging (VMI) to probe collision products has enabled the observation of delicate features in angular scattering distributions.²⁰⁻²³ However, the sparse availability of efficient near-threshold resonance-enhanced multiphoton ionization (REMPI) schemes, a prerequisite for obtaining high-resolution scattering images, still limits the number of systems for which the full potential of this approach can be exploited.

Of particular interest are scattering systems involving multiple interaction potentials with non-adiabatic couplings between them where the Born-Oppenheimer approximation no longer holds. A typical example is the spin-orbit (de-)excitation of ground-state atomic carbon, $C(^3P_j) \rightarrow C(^3P_{j'})$, in collisions with He or H₂.^{24,25} This process is highly relevant for interstellar cloud cooling and plays an important role in chemical modelling of the interstellar medium.^{26,27} To date, several experimental and theoretical studies concerning the collision-induced spin-orbit transitions in $C(^3P_j)$ atoms have been published.^{24,25,28-32} In particular, Bergeat *et al.* reported experimental and theoretical integral cross sections (ICSs) for $C(^3P_0) + \text{He} \rightarrow C(^3P_1/^3P_2) + \text{He}$ collisions.²⁴ The excellent agreement between experiment and theory allowed a detailed description of resonance features in the collision energy dependent ICSs. Although currently unavailable, high-resolution experimental investigations of quantum-state-resolved DCSs for these pro-

cesses could provide even more stringent tests for theory as well as further insight into the underlying scattering mechanisms. The main bottleneck here is the 38 m/s ion recoil intrinsic to the conventional (2+1) UV REMPI detection of $C(^3P_j)$,^{33,34} which would wash out the fine details that can be observed in the experimental scattering distributions.

In this work, we experimentally probed state-resolved DCSs for the spin-orbit de-excitation collision process $C(^3P_1) + \text{He} \rightarrow C(^3P_0) + \text{He}$ with high resolution by the first-time implementation of VUV-based REMPI detection in a crossed beam experiment employing a decelerator and VMI. The C atom is well suited for manipulation using magnetic fields,^{34,35} and thus we used a Zeeman decelerator to prepare velocity-controlled packets of $C(^3P_1)$ atoms with narrow velocity and angular spreads. Despite the challenges arising from the reduced carbon beam density after deceleration and the low VUV power generated by difference frequency mixing, scattered carbon atoms were efficiently detected without ion-recoil by implementing a (1+1') (VUV+UV) REMPI scheme. The resulting exceptional resolution allowed us to fully resolve diffraction oscillations, for which excellent agreement was found with simulations based on *ab initio* calculations of the involved potential energy curves (PECs). Since the use of VUV light for REMPI detection is generally applicable^{36,37} and provides the perspective of recoil-free detection for many atomic and molecular species, this approach offers exciting prospects to study a large range of collision processes with an unprecedented level of precision.

The recoil-free (1+1') (VUV+UV) REMPI scheme for the state-selective detection of $C(^3P_j)$ atoms is schematically depicted in Figure 1 (a). It employs the $2p3s\ ^3P_j \leftarrow 2p^2\ ^3P_j$ transition induced by 166 nm VUV light, which is produced by difference frequency mixing $(2\omega_1 - \omega_2)$ ^{38,39} of co-propagating $\lambda_1 = 212.56$ nm (0.5 mJ) and $\lambda_2 = 296$ nm (0.4 mJ) laser beams focussed inside a gas cell filled with 85 mbar krypton. While this transition is well known from precision spectroscopy experiments,^{40,41} it has not been used for REMPI detection in previous scattering experiments. The ion-recoil associated

with the excess energy of ionization by e.g. a λ_1 or λ_2 photon is generally of no particular importance for spectroscopic investigations. When imaging scattering distributions, however, this ion-recoil induces a velocity blurring that washes out the fine structures that can be observed. Therefore, our implementation, which is similar to that of Glab *et al.*,⁴⁰ uses $\lambda_3 \sim 329$ nm light (8.5 mJ, partially focussed) for subsequent near-threshold ionization that allows for efficient high-resolution imaging of the carbon atoms.

For the VUV excitation step, the $2p3s\ ^3P_1$ intermediate state was chosen to state-selectively detect either the $C(^3P_1)$ from the decelerated beam or the $C(^3P_0)$ scattering product. The UV laser pulses (212, 296 and 329 nm) were generated by frequency doubling or tripling the output of three separate dye-lasers. Optimal time overlap for the 212 and 296 nm laser pulses used to generate VUV light was ensured with the use of a shared Nd:YAG pump laser and suitable delay line. For the 329 nm ionization laser a separate Nd:YAG pump laser was used. The time jitter for each pump laser amounts to less than 1 ns, which is significantly shorter than both the laser pulse duration of around 6 ns full width at half maximum (FWHM) and the expected 2.7 ns lifetime of the $2p3s\ ^3P_1$ intermediate state.^{42,43} The VUV light was not separated from its parent λ_1 and λ_2 UV beams, and was focussed by a MgF₂ lens (focal length ~ 275 mm) at a substantial distance behind the detection region.

When scanning the λ_3 ionization laser wavelength after VUV excitation, see Figure 1 (b), a clear step in the ion yield was observed for the threshold of both the $^2P_{1/2}$ ionic ground state as well as the $^2P_{3/2}$ state of the ion that lies just 63.42 cm⁻¹ higher in energy.⁴⁴ Furthermore, just above the $^2P_{1/2}$ threshold a series of sharp peaks can be observed that correspond to resonant excitation to autoionizing Rydberg states.⁴⁰ While these resonances provide a strong enhancement in signal level just above the ionization threshold, many of them lead to a small increase in blurring of the VMI images. This blurring is attributed to the expected long lifetimes of these Rydberg states in combination with the employed large ionization

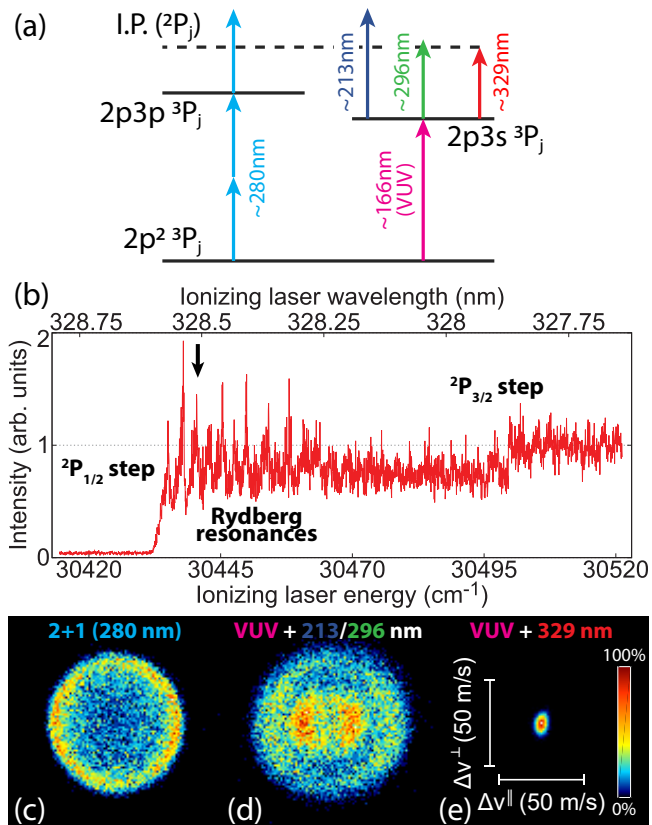


Figure 1: (a) Schematic depiction of the conventional (2+1) REMPI scheme and different competing ionization pathways for the (1+1') REMPI scheme involving VUV excitation. (b) The observed (1+1') REMPI yield as a function of the additional λ_3 ionizing laser wavelength after VUV excitation to the $2p3s\ ^3P_1$ state. The packet of $C(^3P_1)$ atoms exiting the Zeeman decelerator with a mean longitudinal velocity of $v^{\parallel} = 300$ m/s was imaged with the conventional (2+1) REMPI scheme (c), and the (1+1') REMPI scheme both without (d) and with (e) $\lambda_{3,res}$ radiation present. Each image pixel corresponds to a velocity of around 1.2 m/s.

volume (several mm in each dimension), which poses especially demanding conditions for accurate velocity mapping. However, the resonance at $\lambda_{3,res} = 328.5079$ nm, indicated by the arrow in Figure 1 (b), was found to give a significant increase in ion yield while causing only a marginal increase in image blurring. At this peak, the ratio of the signal levels with the $\lambda_{3,res}$ laser on and off was found to be around 33:1, which gives a lower bound for the ratio between signal from low-recoil near-threshold ionization and

the high-recoil contribution from ionization by the λ_1 and λ_2 laser beams co-propagating with the VUV light. It should be noted that separation of the VUV light from its parent UV beams by suitable dichroics should effectively eliminate the high-recoil contribution, and would allow for the use of stronger VUV radiation to increase the ion yield while maintaining low overall recoil.

To illustrate the improvement in image resolution afforded by the implementation of the (1+1') REMPI scheme, the packet of $C(^3P_1)$ atoms exiting the decelerator with a mean longitudinal velocity of $v^{\parallel} = 300$ m/s was velocity map imaged both with and without the addition of the $\lambda_{3,\text{res}}$ laser after VUV excitation, as well as with a conventional (2+1) REMPI detection scheme. The results are depicted in Figure 1 (c - e). For (2+1) REMPI detection, a 280.31 nm laser (10.5 mJ, partially focussed) was used to induce the $2p3p\ ^3P_1 \leftarrow 2p^2\ ^3P_1$ transition and subsequently ionize the atom,^{33,34} as schematically depicted in Figure 1 (a). The image noise arising from the ionization of background gas was found to be strongly increased for (2+1) REMPI detection in comparison with the VUV-based detection schemes. To suppress this noise, the ^{13}C isotope was used when employing the (2+1) REMPI scheme, while the naturally most abundant ^{12}C isotope was used for the images recorded with VUV radiation. Both isotopes are transmitted through the Zeeman decelerator with near-identical efficiency. The laser powers were attenuated for each beamspot image such that less than one ion per shot was recorded on average. The 36 m/s recoil for the (2+1) REMPI detection of ^{13}C causes the ion signal to appear on a ring centered around the mean velocity of the decelerated beam, and with a radius corresponding to the recoil velocity (see Figure 1 (c)). The intensity distribution along the ring depends on the initial orbital of the ejected electrons as well as the laser polarizations. Similarly, when ionizing by λ_1 and λ_2 after VUV excitation, two concentric rings are observed that correspond to ^{12}C recoil velocities of 39 and 17 m/s, respectively (see Figure 1 (d)). By contrast, when employing the $\lambda_{3,\text{res}}$ light for near-threshold ionization after VUV excitation, which reduces the ^{12}C ion-recoil to < 0.9 m/s,

a small and well-defined spot is observed in the VMI image that reflects the velocity spreads of the Zeeman decelerated beam itself (see Figure 1 (e)). The low VUV power generated by difference frequency mixing suppressed the absorption of another VUV photon after VUV excitation, and signals from this high-recoil ionization process could not be distinguished.

The near-threshold (1+1') REMPI scheme implemented here appeared remarkably efficient. The (1+1') scheme provided a similar ion yield as the conventional (2+1) REMPI scheme, while a strong decrease in ionization of background gas was observed. Together, this resulted in a significantly better signal to noise ratio in the scattering images captured with the (1+1') (VUV+UV) detection method. These observations show that, despite the low VUV power, VUV+UV detection as employed here can provide a promising path to recoil-free detection of species for which near-threshold (UV+UV') REMPI schemes are either unavailable or experience strong (UV+UV) competition associated with large ion recoil.

The packets of $C(^3P_1)$ atoms that exit the decelerator with various selected longitudinal velocities (v^{\parallel}) were characterized by recording their time-of-flight (TOF) profiles and by imaging their velocity distributions using VMI in combination with the low-recoil REMPI scheme. The TOF profiles are depicted in Figure 2 and show excellent agreement with the profiles obtained from numerical particle trajectory simulations that take into account the forces exerted on the $C(^3P_1)$ atoms by the space- and time-dependent fields inside our Zeeman decelerator apparatus. The VMI images were recorded at the peaks of the TOF profiles and thus capture the velocity distributions of the most intense part of the packets (see Figure 1 (e) for the example of $v^{\parallel} = 300$ m/s). From these images, the velocity distributions in both the longitudinal (\parallel) and transverse (\perp) direction were extracted and fitted with a Gaussian function. The resulting FWHM velocity spreads are summarized in Table 1 and show good agreement with the values extracted from the simulations.

The well-controlled packets of Zeeman-decelerated $C(^3P_1)$ atoms in combination with

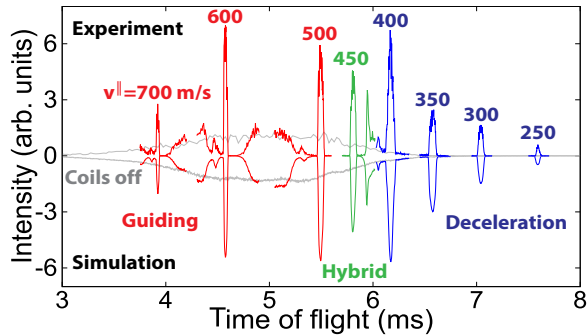


Figure 2: Selected parts of the TOF profiles for $C(^3P_1)$ atoms that exit the decelerator when it is programmed to either guide a packet of $C(^3P_1)$ -atoms at a constant speed (Guiding mode, red) or decelerate a packet with an initial velocity of 500 m/s to various final velocities (Hybrid or Deceleration modes, green and blue, respectively), see Experimental methods for further details. The experimental profiles are shown above the simulated profiles, and the obtained longitudinal velocities (v^{\parallel}) corresponding to the peaks are indicated. The profile recorded with the coils switched off is shown for comparison (gray).

Table 1: Experimental (Exp.) and simulated (Sim.) longitudinal (σ_v^{\parallel}) and transverse (σ_v^{\perp}) FWHM velocity spreads of the packets of $C(^3P_1)$ exiting the Zeeman decelerator with different mean longitudinal velocities (v^{\parallel}). The possible contribution of residual ion-recoil to the experimental velocity spreads is not included in the simulations.

v^{\parallel} (m/s)	FWHM σ_v^{\parallel}		FWHM σ_v^{\perp}	
	Exp.	Sim.	Exp.	Sim.
700	15.6	13.8	10.0	7.3
600	13.4	13.1	9.7	7.4
500	12.2	11.9	11.5	10.4
450	9.2	8.8	10.9	11.7
400	11.7	11.8	7.7	8.6
350	6.7	6.6	8.9	7.3
300	4.8	3.9	7.8	9.9
250	4.1	2.1	8.0	7.2

the efficient low-recoil detection are an ideal starting point for a high-resolution crossed-beam

scattering experiment. To demonstrate this, we recorded scattering images for de-excitation $C(^3P_1) + \text{He} \rightarrow C(^3P_0) + \text{He}$ collisions (see Figure 3 (e)) at three different collision energies (E_{coll}), see Figure 3 (a - c). The images are presented such that the relative velocity vector is directed horizontally, with forward scattering angles positioned at the right side of the image, see Figure 3 (d). Small segments of the images are masked where the initial atomic beam gives a contribution to the signal. Besides the strong scattering ring corresponding to $^3P_1 \rightarrow ^3P_0$ de-excitation, a weak outer ring is observed for the $^3P_2 \rightarrow ^3P_0$ channel, which arises from the significantly lower density of $C(^3P_2)$ that is co-decelerated with the $C(^3P_1)$ atoms. The two rings are well separated due to the high image resolution.

In each of the recorded scattering images, a clear oscillatory pattern can be observed by virtue of the exceptional resolution afforded by the combination of Zeeman-deceleration, VMI and near-threshold ionization used in the experiment.⁴⁵ These oscillations result from the quantum mechanical nature of the atoms that leads to diffraction of matter waves during the collision. The angular scattering distributions, shown in Figure 3 (a-c), are retrieved from the experimental image intensities within a narrow annulus around the observed rings and can be directly compared to the distributions obtained from simulated images. Our image simulations are based on theoretical state-to-state cross sections acquired from quantum mechanical close-coupling (QM CC) calculations that use state-of-the-art *ab initio* C-He PECs,^{24,28,29} in combination with the particle trajectory simulations on our Zeeman decelerator apparatus. The simulated images are shown next to the experimental ones, and are analyzed analogously to their experimental counterparts to acquire predicted angular scattering distributions that take into account the spatial, temporal and velocity spreads of the used atomic beams.^{23,45} Our measurements are in excellent agreement with the simulated distributions, which confirms the high quality of the PECs used in the scattering calculations.

A qualitative understanding of the diffraction

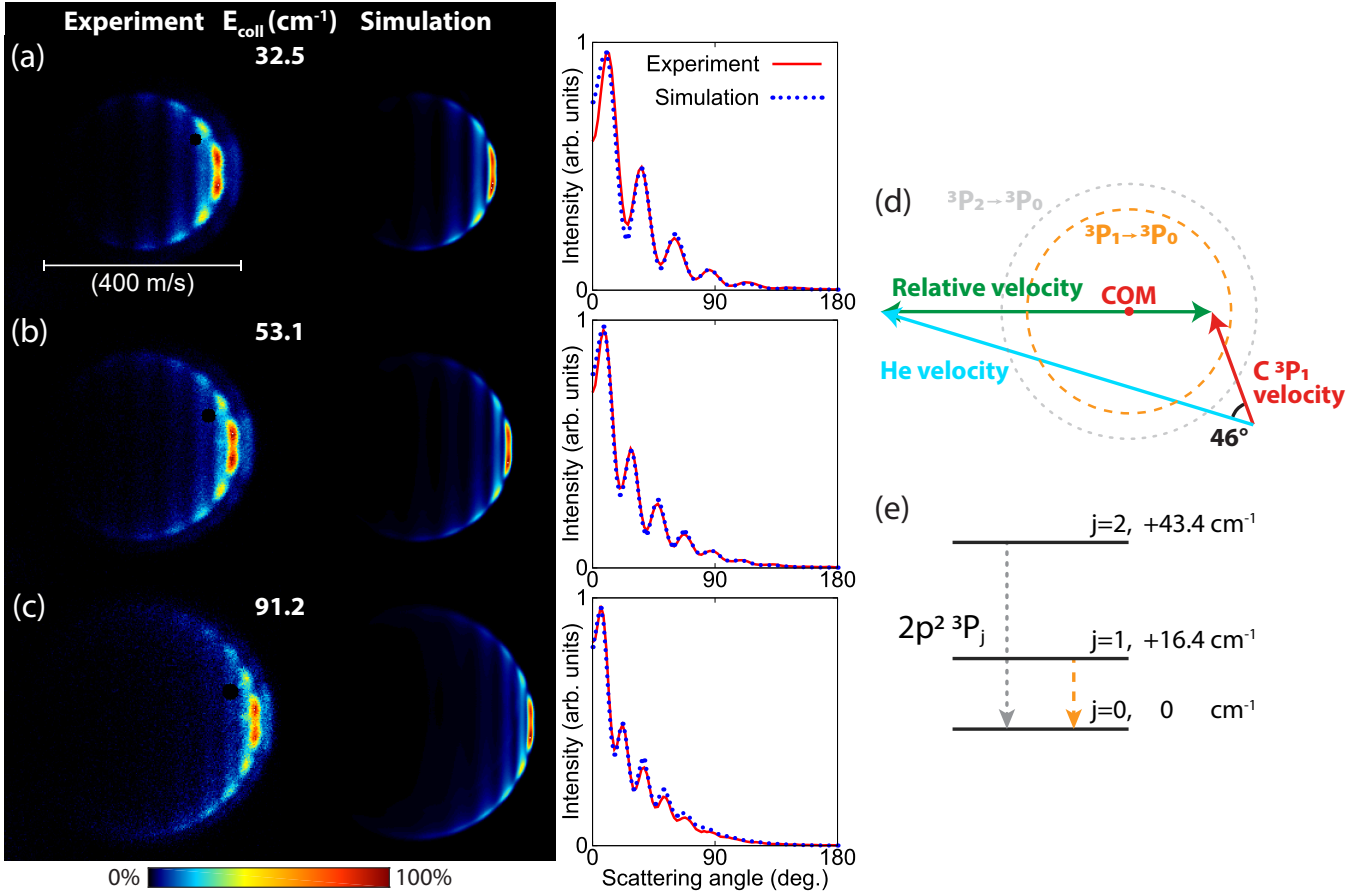


Figure 3: (a)-(c) Experimental and simulated scattering images for the $C(^3P_1) + \text{He} \rightarrow C(^3P_0) + \text{He}$ de-excitation process at three different collision energies, together with the corresponding angular scattering distributions extracted from the bottom half of each image. One image pixel corresponds to a velocity of 2.41 m/s. The weak outer rings in the experimental images correspond to de-excitation from the $C(^3P_2)$ initial state that is significantly less populated in the decelerated beam. Small segments of the experimental images are masked where the initial beam gives a contribution to the signal. (d) Schematic velocity diagram illustrating how the scattered C atoms are projected on a circle around the center of mass (COM). (e) Energy level diagram of the involved $C(^3P_j)$ spin-orbit levels.

oscillations follows from a semi-classical picture in which a matter wave scatters on a structureless target. Within a hard-sphere model, the angular spacing between diffraction peaks can be approximated by $\Delta\theta = \pi/(kR)$, in which k denotes the wavenumber of the incoming wave and R is the radius of the sphere.¹¹ The collision energy is related to k through $\hbar k = \sqrt{2\mu E_{\text{coll}}}$, where μ is the reduced mass of the system. The sphere radius can be determined from the PECs as the C-He distance where the potential energy equals the experimental collision energy. The interaction of $C(^3P)$ with $\text{He}(^1S)$ gives rise to a doubly degenerate PEC of $^3\Pi$ character and a PEC of $^3\Sigma$ character, which are coupled through

the spin-orbit interaction.²⁴ The values for R and the values for $\Delta\theta$ predicted by a hard-shell model using both PECs are given in Table 2 for the collision energies of the experiment, together with the values for $\Delta\theta$ that follow from the QM CC calculations. Qualitative agreement is found, both with respect to the values for $\Delta\theta$ and with respect to the observed trend that $\Delta\theta$ decreases with increasing collision energy.

The ability to experimentally resolve detailed structures like diffraction oscillations in the angular scattering distributions of C + He collisions as demonstrated here shows that the combination of Zeeman deceleration, VMI and near-threshold VUV REMPI detection allows

Table 2: Parameters used for and following from the hard-shell model. For the experimental collision energies (E_{coll}), the radius (R) of the sphere and the angular spacing ($\Delta\theta$) between the diffraction oscillations following from the QM CC calculations and the hard-shell model with the two potential energy curves (PECs) are listed.

E_{coll} (cm $^{-1}$)	32.5	53.1	91.2
R , $^3\Sigma$ PEC (a_0)	5.0	4.8	4.7
R , $^3\Pi$ PEC (a_0)	6.1	5.9	5.6
$\Delta\theta$ hard shell, $^3\Sigma$ PEC ($^\circ$)	28	23	18
$\Delta\theta$ hard shell, $^3\Pi$ PEC ($^\circ$)	23	19	15
$\Delta\theta$ QM CC calculations ($^\circ$)	26	20	15

for high-resolution measurements that provide a sensitive test for theoretical models. The resolution attained here is similar to the resolution achieved in crossed beam experiments that use Stark decelerated NO radicals, which currently defines the state of the art in this type of experiments.^{21,22,45,46}

Our approach opens new vistas to study interesting collision phenomena in a wide variety of systems, for example, the observation of predicted scattering resonances in the ICSs and accompanying rapid changes of structure in the DCSs of low energy $C(^3P_1) + \text{He}^{24}$ as well as $C(^3P_1) + \text{H}_2$ de-excitation collisions.^{28,29} Moreover, inelastic scattering of $C(^3P)$ atoms with complex molecules like O_2 and NO could be investigated to study, for instance, the role of nonadiabatic dynamics when open shell species interact, thus providing a further challenge for theory. Additionally, since a large variety of chemically relevant species is amenable to Zeeman or Stark deceleration¹⁶ and the use of VUV light provides the perspective of recoil-free REMPI detection for many species, the combination of techniques demonstrated here offers new and exciting prospects to study a large range of collision processes with an unprecedented level of precision. Noteworthy species like OH, CO, NH_3 , and CH_3 possess well-known VUV transitions,⁴⁷⁻⁵⁰ although for some the intermediate state is strongly predissociative, and it remains to be seen how efficient and state-selective

near-threshold multi-color REMPI schemes are best implemented for these species. Furthermore, making use of the recently reported near-threshold VUV REMPI schemes for H/D⁵¹ or $\text{O}(^3P)$ atoms,⁵² our approach provides a pathway to high-resolution and low-energy investigations of elementary reactive scattering processes that produce O- or H-atoms, such as $\text{C} + \text{O}_2 \rightarrow \text{CO} + \text{O}$ ^{35,53,54} or complex-forming reactions between Zeeman decelerated atoms and H_2 molecules.⁵⁵⁻⁵⁷

Experimental methods

A beam of carbon atoms, $C(^3P_j)$, with a mean velocity of around 550 m/s was generated by running an electric discharge through an expansion of 2% CO seeded in krypton (see Figure 4), using a Nijmegen Pulsed Valve (NPV) with discharge assembly.⁵⁸ After the expansion, the majority of the carbon atoms resided in the 3P_0 ground state spin-orbit level, while the $^3P_{1,2}$ levels were much less populated. This beam of carbon atoms then passed a skimmer and entered the Zeeman decelerator, of which a detailed description is given elsewhere.⁵⁹ Briefly, it consists of an alternating array of pulsed solenoids and permanent magnetic hexapoles that allow independent control over the longitudinal and transverse motion of paramagnetic species, respectively. The decelerator contains a total of 100 solenoids and 101 hexapoles, and was operated at a repetition rate of 20 Hz. Each coil can be pulsed once to either accelerate or decelerate the packet of C atoms as it passes the coil (Acceleration or Deceleration mode). Double pulses can be used (Hybrid mode), for example to increase contrast in the TOF profiles for mild deceleration or to guide the packet through the decelerator at a constant speed (Guiding).⁵⁹ The C-atom 3P_1 state has a magnetic moment of $1.5 \mu_B$ and splits into $m_j = 0, \pm 1$ components in the presence of a magnetic field, with m_j the projection of the total electronic angular momentum j on the space-fixed z -axis. The $m_j = 1$ component was effectively manipulated with the decelerator. Similarly, the 3P_2 state has a magnetic moment of $3 \mu_B$ and splits

into five components, i.e., $m_j = 0, \pm 1, \pm 2$. Although the $C(^3P_2, m_j = 1, 2)$ components were co-decelerated with the $C(^3P_1, m_j = 1)$ atoms, their density in the beam was significantly lower. While the 3P_0 state had a much higher initial population, it only has an $m_j = 0$ component which is almost insensitive to magnetic fields. The resulting free flight through the decelerator heavily reduced the 3P_0 atom density, such that its final contribution was negligible. Thus, after the decelerator a beam of mainly $C(^3P_1)$ atoms was obtained with controlled velocity and narrow angular and velocity spreads. A series of 13 additional hexapoles guided the packets of $C(^3P_1)$ atoms towards the interaction region, where they were intersected by a beam of He atoms at an angle of 46° about 368.5 mm from the decelerator exit. The He beam was produced using an Even-Lavie Valve (ELV) that was cryogenically cooled to control the mean velocity, thus changing the mean collision energy to 32.5, 53.1, or 91.2 cm^{-1} when intersected by the packets of $C(^3P_1)$ atoms that were decelerated to a final velocity of 350 m/s. After scattering, the product $C(^3P_0)$ atoms were state-selectively ionized using a near-threshold (1+1') (VUV+UV) REMPI scheme, and detected with the use of high-resolution VMI ion optics that allows for accurate mapping of large ionization volumes.⁶⁰ Due to the obtained narrow velocity spreads of the decelerated C atoms the scattering signal arising from the contribution of co-decelerated initial $C(^3P_2)$ could be well separated from the main $C(^3P_1)$ contribution.

Theoretical methods

In a full description of the collision process including the electronic fine-structure of the C atom, the states in the $C(^3P_j)+\text{He}$ arrangement are described by the quantum number j , which corresponds to the total electronic angular momentum of the 3P carbon atom ($\mathbf{j} = \mathbf{L} + \mathbf{S}$ with L and S the electronic orbital and spin angular momenta, respectively). For the calculation of the integral and differential cross sections for the collision of $C(^3P_j)$ with He to give $C(^3P_{j'})$, we used the close coupling approach of Pouilly

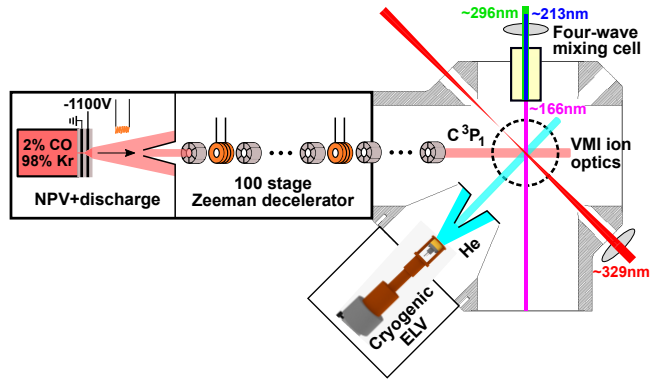


Figure 4: Schematic depiction of the crossed-beam setup. The used combination of Zeeman deceleration, (1+1') (VUV+UV) near-threshold REMPI detection and VMI allowed for high-resolution imaging of C-atom scattering distributions after interaction with He.

*et al.*⁶¹ implemented in the HIBRIDON package.⁶² The calculations were performed with C-He PECs of Bergeat *et al.*²⁴ calculated using the spin-unrestricted single and double excitation coupled cluster approach with non-iterative perturbational treatment of triple excitations (UCCSD(T))⁶³ and an augmented correlation-consistent polarized valence quintuple-zeta (aug-cc-pV5Z) basis set completed with additional 3s 3p 2d 2f 1g mid-bond functions.⁶⁴ The asymptotic experimental spin-orbit splitting of $C(^3P)$ ($A_{SO} = \Delta_{j=1} = 16.41671 \text{ cm}^{-1}$ and $\Delta_{j=2} = 43.41350 \text{ cm}^{-1}$)⁶⁵ was used in the computation of energy levels and in the quantum scattering calculations. In all calculations, the propagation was performed for R ranging from 2.5 to 80 Bohr, with R the interatomic C-He distance. The reduced mass of the C-He complex is $\mu_r = 3.001 \text{ u}$. At each collision energy, the maximum value of the total angular momentum J_{max} was set large enough to converge the integral and differential cross sections within 0.001 \AA^2 . The effective DCSs that were used as input for the image simulations were constructed from the computed DCSs by taking into account the experimental collision energy spreads as a Gaussian distribution.

Acknowledgments

This work is part of the research program of the Dutch Research Council (NWO). This project has received funding from the European Research Council (ERC) under the European Union’s Horizon 2020 research and innovation program (Grant Agreement No. 817947 FICOMOL). It has moreover received funding from the European Union’s Horizon 2020 research and innovation program under the Marie Skłodowska-Curie grant agreements No. 886046 and 889328. We thank Xingan Wang for discussions and support on VUV generation, and David Parker for discussions on REMPI of carbon atoms and careful reading of the manuscript. We thank Niek Janssen, André van Roij and Edwin Sweers for expert technical support.

References

- (1) Levine, R. D.; Bernstein, R. B. *Molecular Reaction Dynamics and Chemical Reactivity*; Oxford University Press: New York, 1987.
- (2) Yang, X., Liu, K., Eds. *Modern Trends in Chemical Reaction Dynamics Part I: Experiment and Theory*; World Scientific: Singapore, 2004.
- (3) Brouard, M., Vallance, C., Eds. *Tutorials in Molecular Reaction Dynamics*; RSC Publishing: Cambridge, 2010.
- (4) Casavecchia, P. Chemical reaction dynamics with molecular beams. *Rep. Prog. Phys.* **2000**, *63*, 355–414.
- (5) Kohguchi, H.; Suzuki, T. State-to-state rotational inelastic scattering of free radicals. *Annu. Rep. Prog. Chem., Sect. C Phys. Chem.* **2002**, *98*, 421–449.
- (6) Le Picard, S. D.; Biennier, L.; Monnerville, M.; Guo, H. In *Gas-Phase Chemistry in Space*; Lique, F., Faure, A., Eds.; IOP Publishing, 2019; pp 3–1 to 3–48.
- (7) Liu, K. Recent advances in crossed-beam studies of bimolecular reactions. *J. Chem. Phys.* **2006**, *125*, 132307.
- (8) Yang, X. Probing state-to-state reaction dynamics using H-atom Rydberg tagging time-of-flight spectroscopy. *Phys. Chem. Chem. Phys.* **2011**, *13*, 8112–8121.
- (9) Naulin, C.; Costes, M. Experimental search for scattering resonances in near cold molecular collisions. *Int. Rev. Phys. Chem.* **2014**, *33*, 427–446.
- (10) Aoiz, F. J.; Brouard, M.; Gordon, S. D. S.; Nichols, B.; Stolte, S.; Walpole, V. A new perspective: imaging the stereochemistry of molecular collisions. *Phys. Chem. Chem. Phys.* **2015**, *17*, 30210–30228.
- (11) Onvlee, J.; Vogels, S. N.; van der Avoird, A.; Groenenboom, G. C.; Van De Meerakker, S. Y. T. Resolving rainbows with superimposed diffraction oscillations in NO + rare gas scattering: experiment and theory. *New J. Phys.* **2015**, *17*, 055019.
- (12) Amarasinghe, C.; Li, H.; Perera, C. A.; Besemer, M.; Zuo, J.; Xie, C.; van der Avoird, A.; Groenenboom, G. C.; Guo, H.; Klos, J. et al. State-to-state scattering of highly vibrationally excited NO at broadly tunable energies. *Nat. Chem.* **2020**, *12*, 528–534.
- (13) Yuan, D.; Huang, Y.; Chen, W.; Zhao, H.; Yu, S.; Luo, C.; Tan, Y.; Wang, S.; Wang, X.; Sun, Z. et al. Observation of the geometric phase effect in the H+HD → H₂+D reaction below the conical intersection. *Nat. Commun.* **2020**, *11*, 3640.
- (14) Chen, W.; Wang, R.; Yuan, D.; Zhao, H.; Luo, C.; Tan, Y.; Li, S.; Zhang, D. H.; Wang, X.; Sun, Z. et al. Quantum interference between spin-orbit split partial waves in the F + HD → HF + D reaction. *Science* **2021**, *371*, 936–940.
- (15) Paliwal, P.; Deb, N.; Reich, D. M.; van der Avoird, A.; Koch, C. P.; Narevicius, E.

- Determining the nature of quantum resonances by probing elastic and reactive scattering in cold collisions. *Nat. Chem.* **2021**, *13*, 94–98.
- (16) van de Meerakker, S. Y. T.; Bethlem, H. L.; Vanhaecke, N.; Meijer, G. Manipulation and control of molecular beams. *Chem. Rev.* **2012**, *112*, 4828–4878.
- (17) Meijer, G. In *Molecular Beams in Physics and Chemistry: From Otto Stern's Pioneering Exploits to Present-Day Feats*; Friedrich, B., Schmidt-Böcking, H., Eds.; Springer International Publishing, 2021; pp 463–476.
- (18) Jansen, P.; Merkt, F. Manipulating beams of paramagnetic atoms and molecules using inhomogeneous magnetic fields. *Progr. Nucl. Magn. Reson. Spectros.* **2020**, *120–121*, 118–148.
- (19) Heazlewood, B. R. Quantum-state control and manipulation of paramagnetic molecules with magnetic fields. *Annu. Rev. Phys. Chem.* **2021**, *72*, 353–373.
- (20) Onvlee, J.; Vogels, S. N.; van de Meerakker, S. Y. T. Unraveling Cold Molecular Collisions: Stark Decelerators in Crossed-Beam Experiments. *Chem. Phys. Chem.* **2016**, *17*, 3583–3595.
- (21) Gao, Z.; Karman, T.; Vogels, S. N.; Besemer, M.; van der Avoird, A.; Groenenboom, G. C.; van de Meerakker, S. Y. T. Observation of correlated excitations in bimolecular collisions. *Nat. Chem.* **2018**, *10*, 469–473.
- (22) de Jongh, T.; Besemer, M.; Shuai, Q.; Karman, T.; van der Avoird, A.; Groenenboom, G. C.; van de Meerakker, S. Y. T. Imaging the onset of the resonance regime in low-energy NO-He collisions. *Science* **2020**, *368*, 626–630.
- (23) Plomp, V.; Gao, Z.; Cremers, T.; Besemer, M.; van de Meerakker, S. Y. T. High-resolution imaging of molecular collisions using a Zeeman decelerator. *J. Chem. Phys.* **2020**, *152*, 091103.
- (24) Bergeat, A.; Chefdeville, S.; Costes, M.; Morales, S. B.; Naulin, C.; Even, U.; Klos, J.; Lique, F. Understanding the quantum nature of low-energy $C(^3P_j) + He$ inelastic collisions. *Nat. Chem.* **2018**, *10*, 519–522.
- (25) Le Picard, S. D.; Honvault, P.; Bussery-Honvault, B.; Canosa, A.; Laubé, S.; Launay, J.-M.; Rowe, B.; Chastaing, D.; Sims, I. R. Experimental and theoretical study of intramultiplet transitions in collisions of $C(^3P)$ and $Si(^3P)$ with He. *J. Chem. Phys.* **2002**, *117*, 10109–10120.
- (26) Bensch, F.; Leuenhagen, U.; Stutzki, J.; Schieder, R. [C I] 492 GHz Mapping Observations of the High-Latitude Translucent Cloud MCLD 123.5+24.9. *Astrophys. J.* **2003**, *591*, 1013–1024.
- (27) Neufeld, D. A.; Lepp, S.; Melnick, G. J. Thermal balance in dense molecular clouds: radiative cooling rates and emission-line luminosities. *Astrophys. J. Suppl. S.* **1995**, *100*, 132–147.
- (28) Bergeat, A.; Morales, S. B.; Naulin, C.; Klos, J.; Lique, F. Quantum Behavior of Spin-Orbit Inelastic Scattering of C-Atoms by D_2 at Low Energy. *Front. Chem.* **2019**, *7*, 164.
- (29) Klos, J.; Bergeat, A.; Vanuzzo, G.; Morales, S. B.; Naulin, C.; Lique, F. Probing Nonadiabatic Effects in Low-Energy $C(^3P_j) + H_2$ Collisions. *J. Phys. Chem. Lett.* **2018**, *9*, 6496–6501.
- (30) Monteiro, T. S.; Flower, D. R. Excitation of [O I] and [C I] fine structure transitions by He and H_2 : a neglected selection rule. *Mon. Not. R. Astron. Soc.* **1987**, *228*, 101–107.
- (31) Lavendy, H.; Robbe, J. M.; Roueff, E. Interatomic potentials of the C-He system - application to fine structure excitation

- of C $^3P(J)$ in collisions with He. *Astron. Astrophys.* **1991**, *241*, 317–320.
- (32) Staemmler, V.; Flower, D. R. Excitation of the C($2p^2\ ^3P_j$) fine structure states in collisions with He($1s^2\ ^1S_0$). *J. Phys. B. - At. Mol. Opt. Phys.* **1991**, *24*, 2343–2351.
- (33) Bergström, H.; Hallstadius, H.; Lundberg, H.; Persson, A. Detection of carbon using amplified laser-induced fluorescence. *Chem. Phys. Lett.* **1989**, *155*, 27–31.
- (34) Jankunas, J.; Reisman, K. S.; Osterwalder, A. Preparation of state purified beams of He, Ne, C, N, and O atoms. *J. Chem. Phys.* **2015**, *142*, 104311.
- (35) Karpov, M.; Pitzer, M.; Segev, Y.; Narevicius, J.; Narevicius, E. Low-energy collisions between carbon atoms and oxygen molecules in a magnetic trap. *New. J. Phys.* **2020**, *22*, 103055.
- (36) Kung, A. H.; Lee, Y. T. In *Vacuum Ultraviolet Photoionization and Photodissociation of Molecules and Clusters*; Ng, C.-Y., Ed.; World Scientific, 1991; pp 487–502.
- (37) Ng, C.-Y. State-to-state spectroscopy and dynamics of ions and neutrals by photoionization and photoelectron methods. *Annu. Rev. Phys. Chem.* **2014**, *65*, 197–224.
- (38) Hilber, G.; Lago, A.; Wallenstein, R. Broadly tunable vacuum-ultraviolet/extreme-ultraviolet radiation generated by resonant third-order frequency conversion in krypton. *J. Opt. Soc. Am. B* **1987**, *4*, 1753–1764.
- (39) Marangos, J. P.; Shen, N.; Ma, H.; Hutchinson, M. H. R.; Connerade, J. P. Broadly tunable vacuum-ultraviolet radiation source employing resonant enhanced sum–difference frequency mixing in krypton. *J. Opt. Soc. Am. B* **1990**, *7*, 1254–1259.
- (40) Glab, W. L.; Glynn, P. T.; Robicheaux, F. High- np Rydberg states of atomic carbon studied through vuv and uv double resonance. *Phys. Rev. A* **1998**, *58*, 4014–4021.
- (41) Lai, K.-F.; Ubachs, W.; De Oliveira, N.; Salumbides, E. J. Fourier-Transform VUV Spectroscopy of $^{14,15}\text{N}$ and $^{12,13}\text{C}$. *Atoms* **2020**, *8*, 62.
- (42) Haar, R. R.; Curtis, L. J.; Kvale, T. J.; Beideck, D. J.; Martinson, I.; Hellborg, R. Lifetimes of excited levels in neutral carbon. *Astron. Astrophys.* **1991**, *243*, 321–326.
- (43) Zheng, N.; Wang, T. Radiative lifetimes and atomic transition probabilities for atomic carbon and oxygen. *Astrophys. J. Suppl. S.* **2002**, *143*, 231–240.
- (44) Moore, C. E. In *Tables of Spectra of Hydrogen, Carbon, Nitrogen, and Oxygen Atoms and Ions*; Gallagher, J. W., Ed.; CRC Press, 1993.
- (45) von Zastrow, A.; Onvlee, J.; Vogels, S. N.; Groenenboom, G. C.; van der Avoird, A.; van de Meerakker, S. Y. T. State-resolved diffraction oscillations imaged for inelastic collisions of NO radicals with He, Ne and Ar. *Nat. Chem.* **2014**, *6*, 216–221.
- (46) Vogels, S. N.; Onvlee, J.; Chefdeville, S.; van der Avoird, A.; Groenenboom, G. C.; van de Meerakker, S. Y. T. Imaging resonances in low-energy NO-He inelastic collisions. *Science* **2015**, *350*, 787–790.
- (47) Beames, J. M.; Liu, F.; Lester, M. I.; Murray, C. Communication: A new spectroscopic window on hydroxyl radicals using UV + VUV resonant ionization. *J. Chem. Phys.* **2011**, *134*, 241102.
- (48) Sun, Z. F.; von Zastrow, A. D.; Parker, D. H. A simple resonance enhanced laser ionization scheme for CO via the $A^1\Pi$ state. *J. Chem. Phys.* **2017**, *147*, 013909.
- (49) Quintero Pérez, M. Preparation of an ultra-cold sample of ammonia molecules for precision measurements. Ph.D. Thesis, Vrije Universiteit Amsterdam, Amsterdam, 2014.
- (50) Teh, W.; Shiu, W.; Zhou, J.; Liu, K. (VUV+UV)-REMPI Detection of the

- Methyl Radical Product in a Crossed-beam Scattering Experiment. *Chin. J. Chem. Phys.* **2002**, *15*, 218–223.
- (51) Yuan, D.; Yu, S.; Chen, W.; Sang, J.; Luo, C.; Wang, T.; Xu, X.; Casavecchia, P.; Wang, X.; Sun, Z. et al. Direct observation of forward-scattering oscillations in the $\text{H}+\text{HD}\rightarrow\text{H}_2+\text{D}$ reaction. *Nat. Chem.* **2018**, *10*, 653–658.
- (52) Wang, X.-D.; Parker, D. H.; van de Meerakker, S. Y. T.; Groenenboom, G. C.; Onvlee, J. Laser ionisation detection of $\text{O}(^3P_J)$ atoms in the VUV; application to photodissociation of O_2 . *Mol. Phys.* **2021**, e1979264.
- (53) Geppert, W. D.; Reignier, D.; Stoecklin, T.; Naulin, C.; Costes, M.; Chastaing, D.; Le Picard, S. D.; Sims, I. R.; Smith, I. W. M. Comparison of the cross-sections and thermal rate constants for the reactions of $\text{C}(^3P_J)$ atoms with O_2 and NO . *Phys. Chem. Chem. Phys.* **2000**, *2*, 2873–2881.
- (54) San Vicente Veliz, J. C.; Koner, D.; Schwilk, M.; Bemish, R. J.; Meuwly, M. The $\text{C}(^3P) + \text{O}_2(^3\Sigma_g^-) \rightarrow \text{CO}_2 \leftrightarrow \text{CO}(^1\Sigma^+) + \text{O}(^1D)/\text{O}(^3P)$ reaction: thermal and vibrational relaxation rates from 15 K to 20 000 K. *Phys. Chem. Chem. Phys.* **2021**, *23*, 11251–11263.
- (55) Aoiz, F. J.; Bañares, L.; Herrero, V. J. Dynamics of insertion reactions of H_2 molecules with excited atoms. *J. Phys. Chem. A* **2006**, *110*, 12546–12565.
- (56) Guo, H. Quantum dynamics of complex-forming bimolecular reactions. *Int. Rev. Phys. Chem.* **2012**, *31*, 1–68.
- (57) Yang, X. State-to-State Dynamics of Elementary Bimolecular Reactions. *Annu. Rev. Phys. Chem.* **2007**, *58*, 433–459.
- (58) Ploenes, L.; Haas, D.; Zhang, D.; van de Meerakker, S. Y. T.; Willitsch, S. Cold and intense OH radical beam sources. *Review of Scientific Instruments* **2016**, *87*, 053305.
- (59) Cremers, T.; Janssen, N.; Sweers, E.; van de Meerakker, S. Y. T. Design and construction of a multistage Zeeman decelerator for crossed molecular beams scattering experiments. *Rev. Sci. Instrum.* **2019**, *90*, 013104.
- (60) Plomp, V.; Gao, Z.; van de Meerakker, S. Y. T. A velocity map imaging apparatus optimised for high-resolution crossed molecular beam experiments. *Mol. Phys.* **2021**, *119:1-2*, e1814437.
- (61) Pouilly, B.; Orlikowski, T.; Alexander, M. H. Fully ab initio dynamics of fine-structure-changing transitions in collisions of $\text{Mg}(3s3p\ ^3P)$ with He. *J. Phys. B* **1985**, *18*, 1953–1967.
- (62) Alexander, M. H.; Manolopoulos, D. E.; Werner, H.-J.; Follmeg, B.; Dagdigan, P. J. ; with contributions by others. Hibridon package, 2011, available at: <http://www2.chem.umd.edu/groups/alexander/hibridon>.
- (63) Knowles, P. J.; Hampel, C.; Werner, H.-J. Coupled cluster theory for high spin, open shell reference wave function. *J. Chem. Phys.* **1993**, *99*, 5219–5227.
- (64) Dunning Jr., T. H. Gaussian basis sets for use in correlated molecular calculations. I. The atoms boron through neon and hydrogen. *J. Chem. Phys.* **1989**, *90*, 1007–1023.
- (65) Haris, K.; Kramida, A. Critically Evaluated Spectral Data for Neutral Carbon (C I). *Astrophys. J. Suppl. S.* **2017**, *233*, 16–36.